Journal of Magnetic Resonance 307 (2019) 106575

Contents lists available at ScienceDirect

Journal of Magnetic Resonance

journal homepage: www.elsevier.com/locate/jmr

Controlling susceptibility mismatch effects, signal lifetimes, and SNR through variation of B_0 in MRI of rock core plugs

Razieh Enjilela, Bryce MacMillan, Michael J. McAloon [1], Oleg V. Petrov [2], Sarah Vashaee, Bruce J. Balcom *

UNB MRI Centre, Department of Physics, University of New Brunswick, Fredericton, New Brunswick E3B 5A3, Canada

ARTICLE INFO

Article history:
Received 8 December 2018
Revised 14 August 2019
Accepted 15 August 2019
Available online 17 August 2019

Keywords:
Signal to Noise Ratio
Susceptibility contrast
Optimum field
Variable field
Core plug imaging
SPRITE
MRI

ABSTRACT

^{1}H relaxometry measurements of petroleum core plugs are commonly performed on low field magnets (<0.5 Tesla) to reduce the influence of magnetic susceptibility mismatch on measurements of the spin-spin relaxation time, T_2. The Signal to Noise Ratio (SNR) of the MR signal, however, generally decreases with lower magnetic fields. Higher magnetic fields (>3 Tesla) are typically employed in small animal MRI studies to improve SNR and image resolution. For many rock core plug samples, susceptibility mismatch effects can be severe at these higher fields leading to decreased T_2 and T_2^*.

In this work we seek an answer to the general question of what is the best field for MRI of rock core plugs, anticipating that it will be both sample and measurement method dependent. Free Induction Decay (FID) relaxation time measurements were undertaken to investigate the conditions under which the SNR in Centric Scan SPRITE (Single Point Ramped Imaging with T_1 Enhancement) MRI measurements is maximized. The image SNR benefits from greater signal at higher fields, but is negatively impacted by the correspondingly shorter signal lifetimes. Depending on the noise regime of the sample, the maximum SNR may be predicted for Centric Scan SPRITE MRI with T_2^* being B_0 field dependent. In this work we describe a series of simple experimental considerations to determine the optimal B_0 field for SPRITE MRI.

Selection of the best field is aided by a new generation of superconducting magnets which allows the experimentalist to readily vary the field strength. Such magnets allow one to experimentally control sample magnetization for high sensitivity MRI measurements of core plug samples, while controlling the effect of susceptibility mismatch on the signal lifetimes.

1. Introduction

Magnetic Resonance (MR) and Magnetic Resonance Imaging (MRI) are utilized in the study of petroleum reservoir rocks because of the sensitivity of MR/MRI to the fluids; water, oil, and gas, which occupy the pore system of the solid matrix [1–6]. These features make MR/MRI measurements an effective approach for analyzing saturated rock core plugs to determine pore system and fluid/matrix properties [7]. Quantitative MR/MRI measurements such as the Centric Scan SPRITE method are well suited to measuring fluid saturation in petroleum reservoir rocks [8].

Low field, 0.05 T, permanent magnets are commonly employed for T_2 relaxation time measurements in petroleum core analysis [9,10]. The low B_0 field limits micro and macro scale susceptibility driven field distortion [9,11]. Such low fields however lead to a reduction in SNR of MR/MRI measurements. Conventional biomedical MRI measurements of small animals are usually performed at much higher magnetic fields (3 T and above). A higher magnetic field provides better SNR and high quality imaging in biological systems which lack significant magnetic susceptibility effects. It should be noted that biomedical imaging problems exist where susceptibility contrast is very pronounced, for example lung imaging [12,13]. In petroleum rock core plugs, however, the magnetic susceptibility differences between the solid matrix and the pore fluid decrease T_2 and T_2^* [1,14] which hinders MRI with traditional methods. This reduction in T_2^* with increasing field, in extreme cases, can prevent detection of the FID based MR/MRI signal entirely due to rapid signal decay within the dead time of the Radio Frequency (RF) probe [15]. The B_0 field distortion due to magnetic susceptibility mismatch scales linearly with B_0 according to simple magnetostatics [16]. However, in the complicated pore structure of a reservoir rock core, it is experimentally believed that internal field gradients scale with $B_0^{3/2}$ [11]. It is important to know the best

* Corresponding author.
E-mail addresses: Razieh.Enjilela@unb.ca (R. Enjilela), bryce@unb.ca (B. MacMillan), Olegvpetrov@yandex.ru (O.V. Petrov), Sarah.Vashaee@unb.ca (S. Vashaee), bjb@unb.ca (B.J. Balcom).
[1] Deceased.
[2] Current address: Faculty of Mathematics and Physics, Department of Low-Temperature Physics, Charles University, Prague CZ-180 00, Czech Republic.

https://doi.org/10.1016/j.jmr.2019.106575
1090-7807/

choice of B_0 field for core plug MRI studies to balance greater sensitivity at high fields with T_2^* and T_2 reduction as the field increases.

A decrease in the T_2^* lifetime due to susceptibility contrast manifests itself in a decreased image intensity in pure phase encoding Centric Scan SPRITE MRI [1]. In frequency encoding methods such as the Fast Spin Echo (FSE), reduced relaxation lifetimes due to internal magnetic field gradients result in a loss of image intensity and decreased image resolution [17]. 3D Centric Scan SPRITE [8] is a very robust and flexible method employed to study a wide range of core plug systems with short transverse signal lifetimes [18]. As a pure phase encoding technique, SPRITE is largely immune to image distortion due to susceptibility contrast, chemical shift, and paramagnetic impurities. MR/MRI measurements of core plugs [1,6,11] show that the signal decay rate ($1/T_2^*$) is often dominated by the susceptibility mismatch between the solid matrix and the pore fluid, resulting in a single exponential T_2^* decay that inversely scales with the B_0 magnetic field. This occurs even when T_1 and T_2 are multi exponential due to a distribution of pore sizes [7]. The single exponential T_2^* behavior of fluid saturated rock cores is important to the success of quantitative imaging of local fluid content in Centric Scan SPRITE imaging since the local image intensity has simple T_2^* contrast [6].

The SNR is linearly dependent on the applied magnetic field B_0 [19–21] in MR measurements when sample noise dominates. The SNR varies with $B_0^{7/4}$ however when coil noise dominates [19,22]. Doty et al. [23] reported that when the sample noise and coil noise are similar, the SNR will vary as $B_0^{3/2}$. Doty defined mid-range coils, with similar sample and coil noise, as those where the product of the Larmor frequency and coil diameter are in the range 2–30 MHz m. SNR variation with B_0 field for different noise regimes is discussed further in Section 3.1.

In this work, we investigate the variation of $1/T_2^*$ for a wide range of B_0 fields in Section 5.1. The linearity of $1/T_2^*$ versus magnetic susceptibility mismatch, through consideration of multiple rock core plugs, is discussed in Section 5.2. Based on the noise regime, we then determine conditions through which the SNR is maximized in Centric Scan SPRITE MRI. Choice of the optimum field, described in Section 5.3, is facilitated by a new generation of superconducting magnets which allow the field to be readily varied. These magnets allow one to utilize the optimal magnetic field, taking into account sensitivity, the effect of susceptibility mismatch on the signal lifetimes, and resolution.

While the T_2^* variation with field is different for each rock core described in this paper, a series of simple experimental considerations permit one to determine the optimal B_0 field for SPRITE MRI.

2. Methods

2.1. 3D Centric Scan SPRITE

Centric Scan SPRITE MRI employs pure phase encoding and permits quantitative imaging of samples with short T_2^*, often associated with fluids in porous systems [18,24,25]. Fig. 1 depicts the pulse sequence for 3D Centric Scan SPRITE. A short duration broadband RF pulse is applied at each gradient step. The rectangular phase gradients G_x and G_y were stepped sinusoidally while G_z is ramped in a stepped linear fashion through a discrete set of gradient amplitudes. The 3D Centric Scan SPRITE methodology [10,11] employs a series of gridded spiral trajectories along conical surfaces to sample k-space.

Image intensity in a Centric Scan SPRITE image is given by:

$$S = \rho_0 \exp\left(\frac{-t_p}{T_2^*}\right) sin\alpha \tag{1}$$

where ρ_0 is the proton density, t_p is the phase encoding time, T_2^* is the effective spin-spin relaxation time, and α is the flip angle.

3. Theory

3.1. Dependence of SNR on the applied magnetic field B_0

SNR is defined as the ratio of the MR/MRI signal intensity to the standard deviation of signal noise. The SNR in MR images depends on the sample to be imaged and the MR/MRI instrument. It is well

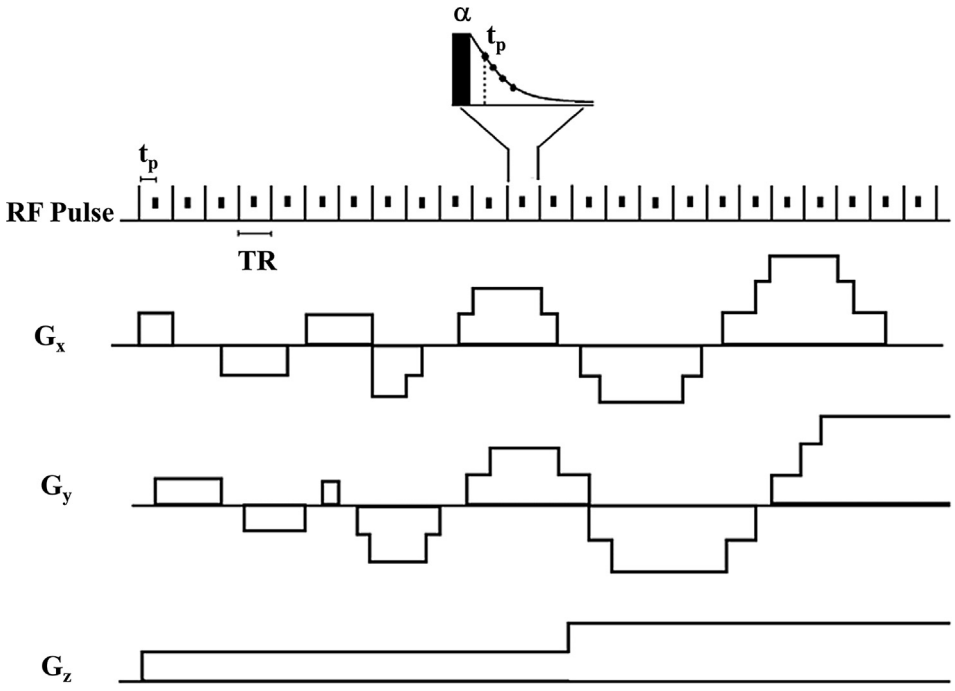

Fig. 1. Pulse sequence diagram for 3D Centric Scan SPRITE. The FID point is acquired at a fixed encoding time (t_p) after the application of a broadband RF pulse in the presence of stepped gradients (G_x, G_y, G_z). TR is the repetition time.

known that the main sources of noise are the RF coil resistance and losses in the sample. The signal intensity after applying the initial RF pulse is proportional to the square of the magnetic field B_0 through Eq. (2) [20,22]

$$S \propto B_0^2 \tag{2}$$

The signal noise can be represented via:

$$S_{Noise} = \sqrt{4kTR_{eff}BW} \tag{3}$$

where k is Boltzmann's constant, T is the absolute temperature in Kelvin [22,26], BW is the receiver bandwidth, and R_{eff} is the effective series resistance.

The principal source of noise in most clinical MRI measurements is the sample to be imaged, with the receiver coil typically a secondary source ($R_{eff} = R_{coil} + R_{sample}$ in Eq. (3)). If sample noise dominates, the noise is proportional to B_0 ($\sqrt{R_{eff}} \propto \sqrt{R_{sample}} \propto B_0$) [19,20]. The SNR, through Eqs. (2) and (3) is thus predicted to vary linearly with B_0 [19,20,27]. If coil noise dominates, ($\sqrt{R_{eff}} \propto \sqrt{R_{coil}} \propto B_0^{1/4}$), SNR is predicted to vary as $B_0^{7/4}$ [19,22]. When the coil and sample losses are both significant (mixed noise regime) in MR measurements, the SNR varies as $B_0^{3/2}$ [23,28]. Radiation resistance is negligible in the core plug imaging considered in this work since the size of the sample and RF coil are much less than the RF wavelength [22,29].

3.2. Single exponential T_2^* decay

The utility of Centric Scan SPRITE techniques is significantly increased due to the single exponential T_2^* behavior frequently observed in porous media. The T_2^* lifetime may be determined through bulk FID measurements where the decay rate ($1/T_2^*$) can be represented by:

$$\frac{1}{T_2^*} \approx \frac{1}{T_2} + \gamma \Delta B_0 + \gamma \Delta \chi B_0 \equiv \frac{1}{T_2} + \frac{1}{T_{2m}} + \frac{1}{T_{2i}} \tag{4}$$

where $1/T_2$ is the spin–spin relaxation rate, γ is the gyromagnetic ratio, $1/T_{2m}$ is the decay rate due to underlying B_0 inhomogeneity (ΔB_0) in the main magnetic field, and $1/T_{2i}$ is the decay rate due to internal field inhomogeneities induced by the susceptibility difference ($\Delta\chi$) between the solid matrix and the pore fluid. In all the core plug samples considered in this study, $T_2 \gg T_{2m}$, T_{2i} and T_2 can be therefore neglected in Eq. (4) [3]. The term ($1/T_{2m}$) in Eq. (4), associated with field inhomogeneity in the magnet, is usually insignificant in realistic core plug samples [1,25]. However, at lower permanent magnet fields, $1/T_{2m}$ may be comparable to $1/T_{2i}$. The value of the term $1/T_{2m}$ can be reduced by shimming the magnet before MR measurement. In most sedimentary rock samples, the T_2^* decay is dominated by $\gamma\Delta\chi B_0$ in Eq. (4) [1,30], which results in an effective single exponential T_2^* lifetime in core plugs. The single exponential behavior of T_2^* implies that the magnetic field distribution is Lorentzian in the pore space [1].

4. Experimental

4.1. Data processing

Home built data processing and visualization programs, Unisort (version 4.43, written in IDL, ITT, Boulder, CO, US) and ACCISS (version 9.1 written in MATLAB, MathWorks, Natick, MA, US), were employed for image reconstruction and display.

4.2. Equipment

MR/MRI measurements employed a cryogen free variable field superconducting magnet operating at 0.79 T, 1.5 T, and 3 T (MR Solutions, Guildford, UK) with ^{1}H resonance frequencies of 33.6 MHz, 63.6 MHz, and 127.8 MHz, respectively. The three RF probes (MR Solutions, Guildford, UK) employed were birdcages, 9 cm in length and 5 cm in diameter, driven by a 2 kW, BT02000-AlphaSA, RF amplifier (TOMCO Technologies, Sydney, Australia). The gradient coil, model BFG 155/100 s-6 (Resonance Research, Billerica, MA, US) was driven by GA-300 gradient amplifiers (Performance Controls, Montgomeryville, PA, US), providing maximum gradient strengths of 66.4 G cm^{-1}, 64.9 G cm^{-1} and 87.8 G cm^{-1} in the x, y and z directions, respectively. The magnet was permanently connected to a 4G superconducting magnet power supply (Cryomagnetics, Oak Ridge, TN, US).

MR/MRI measurements were also performed at 0.2 T with a MARAN DRX-HF (Oxford Instruments, Abingdon, UK) console at a resonance frequency of 8.5 MHz. The instrument was equipped with three Techron gradient amplifiers (Type 7782, AE Techron, Elkhart, IN, US), which provided maximum magnetic field gradients of 25.7 G cm^{-1}, 24.7 G cm^{-1} and 33.7 G cm^{-1} in the x, y, and z directions, respectively. The RF probe was a homemade vertical solenoid 12 cm in length with a 4.4 cm inner diameter. The RF probe was driven by a 1 kW, BT01000-AlphaS, RF amplifier (TOMCO Technologies, Sydney, Australia).

Mass magnetic susceptibility measurements were undertaken with a Johnson-Matthey magnetic susceptibility balance, MSB MK1 (Sherwood Scientific, Cambridge, UK). This balance employed the Evans modification to the original Gouy balance by measuring the force exerted on a suspended permanent magnet when the sample is introduced [31].

RF probe quality factors were measured with a network analyzer (Hewlett Packard HP 8714B, Santa Rosa, CA, US) at room temperature. The quality factor was evaluated based on the frequency response of the RF probe at −3 dB attenuation points [32].

4.3. Bulk FID and 3D Centric Scan SPRITE measurements of saturated core plugs

Bulk FID and 3D Centric Scan SPRITE measurements were undertaken on five rock core plugs, Bentheimer, Nugget, Buff Berea, Berea (Kocurek Industries, Caldwell, TX, US), and Wallace (Wallace Quarries, Wallace, NS, Canada), at 0.2 T, 0.79 T, 1.5 T and 3 T. Core plugs were saturated with 2% NaCl H_2O solutions in a container connected to a vacuum pump and stored under brine between measurements. Physical properties of the brine saturated cylindrical rock core plug samples are reported in Table 1. Each sample was wrapped in Teflon tape to avoid evaporation during measurement.

Bulk FID measurement was undertaken on 11 additional water saturated rock core plugs at a range of magnetic field strengths (Table 2). Mass magnetic susceptibilities were measured on seven of these rock core plugs. Rock samples were ground with a mortar and pestle and dried in a vacuum oven at 65° for several hours prior to susceptibility measurement.

Bulk FID measurement parameters for core plugs at 0.79 T, 1.5 T, and 3 T were: signal averages = 32, spectral width = 400 kHz, RF probe dead time = 10 μs, and flip angle = 11°. The repetition times (TR) were 3.5 s, 0.75 s, 1 s, 0.3 s, and 0.5 s for Bentheimer, Nugget, Buff Berea, Berea, and Wallace core plugs, respectively. The broadband 90° pulse duration was 40 μs at 1.5 T and 33 μs at 3 T. Bulk FID parameters at 0.2 T were: signal averages = 32, filter width = 500 kHz, RF probe dead time = 15 μs. The repetition times were 6 s, 0.6 s, 1.7 s, 1.3 s, and 0.6 s for Bentheimer, Nugget, Buff Berea, Berea, and Wallace core plugs, respectively. The 90°

Table 1
Physical properties of the five core plugs saturated with 2% brine. T_1 relaxation times, measured at 0.2 T, were fit to a bi-exponential model.

Brine saturated Rock cores	Porosity %	Diameter (cm)	Length (cm)	Laminated[a]	Bi-exponential T_1 (ms) at 0.2 T[b]
Bentheimer	24	3.8	5.0	No	73 (11%), 1100 (89%)
Nugget	15	3.8	5.0	Yes	21 (24%), 240 (75%)
Buff Berea	21	3.8	5.0	No	24 (23%), 340 (77%)
Berea	19	3.8	5.0	No	7.0 (27%), 99 (73%)
Wallace	14	3.8	5.0	No	11 (40%), 180 (60%)

[a] Reported lamination is based on visual appearance.
[b] T_1 is modelled as a biexponential for simplicity of reporting.

Table 2
The slope values, $\frac{d(\Delta f_0)}{df_0}$, from a linear fit to the data of $\Delta f_0 = 1/(\pi T_2^*)$ over a range of frequencies, f_0. The slope values differ for each sample due to different magnetic susceptibilities. The volume magnetic susceptibility of a subset of seven core plugs was calculated based on their mass magnetic susceptibility, internal and inter particle porosity, and the rock matrix density.

Sample	Slope of the line $\frac{d(\Delta f_0)}{df_0}$ (10^{-4})	Porosity (%)	Volume susceptibility of matrix (10^{-6} c.g.s)
Rock 174S	1.1	14	−0.75
Rock MT1	0.31	29	0.29
Rock 132B	3.5	–	–
Rock 39A	1.4	13	0.88
Rock CVNS	3.1	–	–
Rock 74B	3.5	–	–
Rock 92A	4.7	22	7.3
Rock 4	3.9	25	13
Rock W001	8.0	14	14
Rock 18A	7.4	19	15
Rock 9B	6.0	–	–

pulse duration was 11.1 μs while the dwell time was 2 μs in all measurements at 0.2 T.

3D Centric Scan SPRITE imaging parameters at 1.5 T and 3 T were: signal averages = 8, spectral width = 200 kHz, RF probe dead time = 10 μs, field of view = 100 × 100 × 100 mm^3, phase encoding time (t_p) = 100 μs, TR = 1 ms, and the maximum magnetic field gradient strength was 7.5 G cm^{-1} in the x, y, and z directions. Gradient switches were abrupt with no shape pulse programmed for the transition. The T_1 recovery delay = 2 s, 500 ms, 680 ms, 200 ms and 360 ms with a total imaging time of 30.0 min, 22.4 min, 23.3 min, 20.8 min, and 21.7 min for Bentheimer, Nugget, Buff Berea, Berea and Wallace core plugs, respectively. The broadband 90° pulse duration was 40 μs at 1.5 T and 34 μs at 3 T. The RF flip angle was 10° for all SPRITE measurements. An additional 3D Centric Scan SPRITE measurement was performed for the Wallace core plug at 3 T with 64 signal averages. With a 360 ms T_1 recovery delay, the total imaging time was 2.8 h for this measurement. No image post processing was undertaken except for image normalization described below.

SPRITE core plug images at 1.5 T and 3 T were normalized to a 3D Centric Scan SPRITE image of a uniform agar gel sample doped with $CuSO_4$, 5 cm in diameter and 10 cm in length. The gel sample was larger than the core plugs, so that the edges of the core plug may be properly normalized. Normalization ensures that variation in the signal intensity in the core plug images is not due to spatial variation of the RF probe sensitivity. Normalization was not undertaken for the 3D SPRITE image of the Wallace sample (with 64 signal averages) at 3 T. The SPRITE imaging parameters for the agar gel sample were the same as those for the core plug images except for the T_1 recovery delay, which was 1 s for the agar gel sample.

3D Centric Scan SPRITE imaging parameters at 0.2 T for the Wallace sample were: signal averages = 64, filter width = 500 kHz, RF probe dead time = 15 μs, dwell time = 2 μs, field of view = 100 × 100 × 100 mm^3, RF flip angle = 10°, t_p = 100 μs, and T_1 recovery delay = 2 s with a total imaging time of 5.6 h. The broadband 90° pulse duration was 11.1 μs. Gradient switches were abrupt with no shape pulse programmed for the transition. No image post processing was undertaken.

The SNR for SPRITE images was calculated in the image domain. The signal was calculated as the mean value of the image magnitude within a region-of-interest (ROI), excluding any blurred edges. The noise was estimated as the standard deviation of the background noise magnitude. The sensitivity was calculated as SNR/$\sqrt{t}$ where t is the total measurement time.

5. Results and discussion

5.1. Bulk FID measurement and prediction of optimum field

Bulk FID measurements were undertaken on the five brine saturated reservoir rock core plug samples listed in Table 1, at 0.2 T, 0.79 T, 1.5 T, and 3 T. The FID data were fit to a single exponential T_2^* decay. Fig. 2 shows a typical bulk FID, from the brine saturated Nugget core plug, after RF excitation at 3 T. The best fit-line is a single exponential with a T_2^* of 280 μs. Single exponential behavior was observed in all core plugs under study. The T_2^* lifetime values are reported in Table 3 for the different field strengths. Bulk T_1 measurement revealed short and long lifetime components for the five core plugs, Table 1, when fitted to a simple biexponential model. Employing a biexponential model permits one to tabulate T_1 lifetimes and their associated signal intensities.

Fig. 3a shows the variation of $1/T_2^*$ over the range of field strengths employed (0.2 T, 0.79 T, 1.5 T, and 3 T) for the brine saturated rock core plugs of Table 1. The data points fall on straight lines based on Eq. (5),

$$\frac{1}{T_2^*} = mB_0 + b \tag{5}$$

The slope m, is determined by susceptibility contrast for each rock sample [1]. The intercept values, b, of individual lines in Fig. 3a agree within experimental error. If surface relaxation is neglected, the straight lines of Fig. 3a will have a common inter-

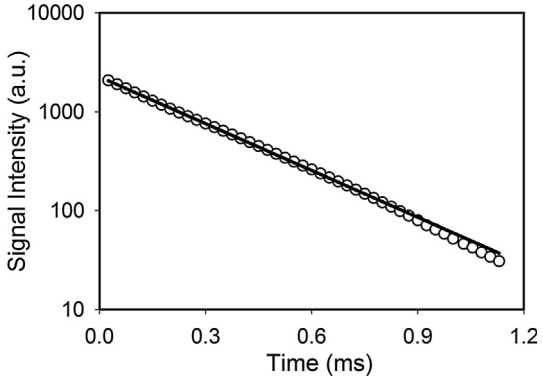

Fig. 2. Semilog plot of the bulk FID signal intensity versus time after RF excitation for a fully brine saturated Nugget sandstone at 3 T (○). The solid line indicates the best fit to a single exponential decay with a T_2^* of 280 μs.

Table 3
T_2^* lifetime of the five core plugs saturated with 2% brine measured at 3 T, 1.5 T, 0.79 T, and 0.2 T.

	T_2^* (μs)			
Sample	3 T	1.5 T	0.79 T	0.2 T
Bentheimer	580 ± 2	1400 ± 2	1900 ± 3	3100 ± 3
Nugget	280 ± 1	410 ± 1	580 ± 3	1900 ± 3
Buff Berea	240 ± 1	310 ± 1	440 ± 2	1700 ± 3
Berea	98 ± 1	170 ± 1	250 ± 1	1100 ± 2
Wallace	34 ± 1	57 ± 1	110 ± 2	390 ± 2

cept which may be estimated by the T_2 of bulk water at low field. The $1/T_2$ of pure water was 0.0004 (ms^{-1}) at 0.05 T. The experimental result of Fig. 3a provides a means to predict the optimal field to maximize the SNR in a Centric Scan SPRITE image. The single exponential behavior observed, and its scaling with B_0, is a simple consequence of inhomogeneous broadening due to susceptibility mismatch in the pore space [1]. Molecular diffusion is not considered, nor it is required, in this simple and successful model of the linewidth [1].

Considering Eqs. (1) and (4) with SNR ∝ B_0, the regime when sample losses dominate, the SNR in a SPRITE measurement will be given by the proportionality of Eq. (6):

$$SNR \propto B_0 \exp(-t_p(mB_0 + b)) \tag{6}$$

The estimated maximum SNR is calculated by zeroing the first derivative of Eq. (6) with respect to B_0.

This yields:

$$B_{0\ max} = \frac{1}{mt_p} \tag{7}$$

Assuming susceptibility contrast determines the field dependence of $1/T_2^*$, the estimated maximum SNR in a Centric Scan SPRITE MRI experiment is predicted to occur when $t_p = T_2^*$ in the sample noise regime. This assumes the intercept is effectively zero and the product of B_0 and slope m is equal to $1/T_2^*$ according to Eq. (5). Graphically, B_{0max} will correspond to the intersection of the $1/T_2^*$ plot with a horizontal line drawn at $1/T_2^* = 1/t_p$ (Fig. 3a).

A typical Centric Scan SPRITE phase encoding time t_p is 100 μs. For the Wallace sandstone, the optimal field is predicted to be 0.92 T. Maximum SNR is, however, not the only concern in MRI core plug measurement. In rock core plug studies one seeks, in the first instance, a quantitative measure of fluid content. The $t_p = T_2^*$ condition results in significant contrast (e^{-1}) and impairs one's ability to generate a quantitative fluid content image. For more quantitative imaging $t_p \ll T_2^*$ is recommended with the

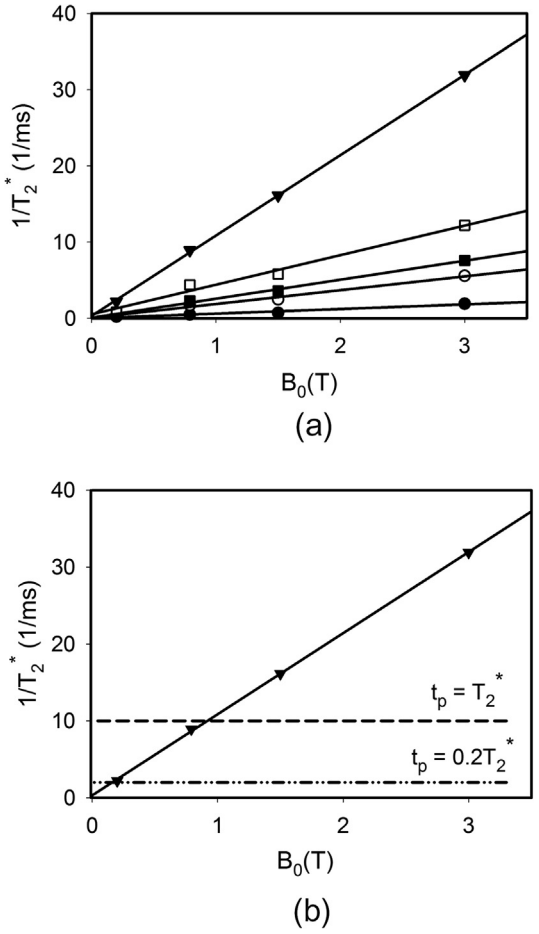

Fig. 3. (a) Variation in the signal decay rate, $1/T_2^*$, as function of B_0 for five brine saturated core plugs at 0.2 T, 0.79 T, 1.5 T, and 3 T. Each core plug [(●) Bentheimer, (○) Nugget, (■) Buff Berea, (□) Berea, and (▼) Wallace] gives a linear dependence. **(b)** $1/T_2^*$ versus B_0 for the Wallace core plug at the above magnetic fields. The upper dashed (- - -) horizontal line corresponds to $T_2^* = t_p$ assuming the sample noise regime. The point of intersection indicates the best choice of field for maximum SNR. The lower horizontal line (-..-..) illustrates $t_p = 1/5\ T_2^*$ where intersection at a lower field yields increased T_2^*, which is beneficial for quantitative imaging. Predictions for the coil noise and mixed noise regimes are not shown.

intersection point in Fig. 3a thereby shifted to lower field due to the required increase in T_2^*, with t_p constant.

The new intersection point for the Wallace sandstone corresponds to 0.16 T when T_2^* is a factor of 5 less than t_p. If one wishes to be more conservative and reduce T_2^* contrast still further one could choose T_2^* less than t_p by a factor of 10 with a resultant further decrease in B_0. The minimum t_p is based on the maximum magnetic field gradient strength available. It is easier to change the t_p, T_2^* inequality by changing the static field strength to change T_2^*. The slope m, for any rock core plug of interest, in a plot similar to that of Fig. 3a, may be simply estimated with the assumption of $b \approx 0$. In this case, a measurement of $1/T_2^*$ at one field B_0 permits direct estimation of the slope of the line.

For the other two noise regimes (coil noise dominated and the mixed noise regime), Eq. (6) may be reformulated with a different power dependence on B_0. A similar differentiation permits one to predict the most appropriate field to maximize SNR in Centric Scan SPRITE images. Note that the rate $1/T_2^*$ as a function of field B_0 does not depend on the noise regime. The same plot (Fig. 3b) can be used to consider the other two noise regimes for the Wallace sandstone. Horizontal lines drawn to determine the optimal B_0 will change with the noise regime.

If the coil noise regime dominates, $t_p = 1.75\,T_2^*$ and B_{0max} will correspond to the intersection of the $1/T_2^*$ plot (Fig. 3b) and a horizontal line drawn at $1/T_2^* = 1/(0.57t_p)$ with $B_{0max} = 1.6$ T for the Wallace sandstone. For the mixed noise regime, with $t_p = 1.5\,T_2^*$, the horizontal line will be set to $1/T_2^* = 1/(0.67t_p)$ for the Wallace sandstone yielding $B_{0max} = 1.4$ T. To reduce T_2^* contrast as outlined previously, with $t_p = 1/5\ T_2^*$, the predicted fields are 0.3 T for the coil noise regime and 0.27 T for the mixed noise regime for Wallace sandstone. Similar plots and calculations are possible for other core plug samples to predict the optimal magnetic fields.

Given the discussion above, there is clear merit in determining the noise regime for a particular core plug and B_0 field. Given the RF probe sizes and frequencies for ^{1}H with the variable field magnet, it was anticipated that the mixed noise regime would be most appropriate for all core plug samples. The RF probes supplied with the MR Solutions magnet have fixed tuning and matching, with a low quality factor, since they are intended as generic rat imaging probes. For all three RF probes, (33.6 MHz, 63.6 MHz, and 127.8 MHz) sample insertion did not change the RF probe quality factor, it remained 58, 40, and 66, respectively at the three frequencies.

The lack of change in the quality factor with sample insertion shows that our MR/MRI measurements are in the coil noise dominated regime with these RF probes. This occurs despite the high salt content in the brine solution. Noise from FID measurements, with and without a core plug sample, was also constant. Control measurements were undertaken with an optimized RF probe, with variable tuning and matching, for a conventional superconducting magnet at 100 MHz. A significant quality factor change resulted upon core plug insertion, suggesting mixed noise regime behavior. Measurements on the variable field magnet in this work are coil noise dominated due to the RF probe design and construction.

A new generation of cryogen free superconducting magnets have the flexibility of variable field operation since they are permanently connected to the magnet power supply. This is particularly advantageous when working with rock core plugs as it allows one to maximize sample magnetization while controlling susceptibility mismatch effects. Once T_2^* has been determined at a single field, the optimal field may be selected given knowledge of the noise regime. Practical experimentation is still subject to the availability of excitation/detection circuitry at the chosen magnetic field.

Bulk FID measurements have been undertaken as part of this work on a wide variety of water saturated core plug samples, Table 2, over a range of field strengths (0.35 T, 2.4 T, 4.8 T, and 7 T). Single exponential T_2^* behavior was observed in all water saturated core plugs as expected [1,3,18]. The linear dependence of $1/T_2^*$ versus B_0 (results not shown) was confirmed for all samples under study. The slope differs for each sample due to different magnetic susceptibility contrast (Table 2). A steeper slope corresponds to a sample with greater magnetic susceptibility mismatch between the matrix and pore fluid.

5.2. Magnetic susceptibility measurement and the effect of $\Delta\chi$ on $1/T_2^*$

The data of the previous section shows that $1/T_2^*$ is proportional to B_0 for a wide range of rock core plugs over a range of fields. Individual samples have different slopes due to presumed differences in $\Delta\chi$. In this section we examine the $\Delta\chi$ dependence of Eq. (4) through variation of the sample.

Mass magnetic susceptibility measurements were undertaken for seven of the air dry core plug samples of Table 2. The measured mass magnetic susceptibility is an average of the mass susceptibilities of the rock matrix and air which is given by:

$$\chi_g = \chi_{g,m} \times p_m + \chi_{g,air} \times p_{air} \tag{8}$$

where $\chi_{g,m}$ is the mass susceptibility of the rock matrix, $\chi_{g,air}$ is the mass susceptibility of air while p_m and p_{air} are the volume fractions of the rock matrix and air, respectively. The volume fraction of the rock matrix is given by:

$$p_m = (1 - \varphi_1) \times (1 - \varphi_2) \tag{9}$$

where φ_1 is the internal porosity of the rock samples and φ_2 is the inter particle porosity (distance between the grains for ground samples). The mass susceptibility of the rock matrix is thus:

$$\chi_{g,m} = \frac{\chi_g}{(1 - \varphi_1) \times (1 - \varphi_2)} \tag{10}$$

the inter particle porosity, φ_2, has been assumed to be 0.36 (as for randomly packed spheres) for all samples. The internal porosity φ_1 was known independently for the seven core plug samples.

The field offset distribution ΔB_0 is determined by the difference in volume susceptibility of the pore fluid and the rock matrix. To obtain the dimensionless rock matrix volume susceptibility $\chi_{v,m}$ (c.g.s units), the rock matrix mass susceptibility values were multiplied by the density of the rock matrix d_m. An average density of 2.3 g/cm^3 [33] was assumed for all sandstone core plug samples. The difference between the volume magnetic susceptibility of the rock matrix and that of water, $\chi_{water} = -0.719 \times 10^{-6}$ c.g.s, was computed for the seven rock core plugs. The difference $\Delta\chi_v$ is reported in Table 2.

Based on Eq. (4), the FID decay rate and the corresponding linewidth, $\Delta f_0 = 1/(\pi T_2^*)$, in a porous rock core plug may be estimated by [1,3]:

$$\Delta f_0 \approx \frac{1}{\pi T_{2i}} \approx \frac{\gamma \Delta B_0}{\pi} \tag{11}$$

where ΔB_0 is the breadth of the magnetic field distribution in the pore space which is proportional to the susceptibility difference and to the field B_0. Thus, $\Delta B_0 = C\Delta\chi B_0$ where C is a dimensionless constant [1]. Considering Eq. (11) and the Larmor equation, a simple expression for Δf_0 results

$$\Delta f_0 \approx \frac{1}{\pi T_{2i}} = \frac{\gamma \Delta B_0}{\pi} = C\Delta\chi f_0 \tag{12}$$

where $f_0 = \frac{\gamma B_0}{2\pi}$ is the Larmor frequency.

The experimental MR linewidth, Δf_0, of the 11 water saturated core plugs of Table 2 depends linearly on field B_0 and thereby frequency f_0 (results not shown). The proportionality constants, i.e. the slope of the lines, vary between core plugs due to the different magnetic susceptibilities. These slopes are reported in Table 2. The volume susceptibilities are known for 7 of the 11 core plugs, Table 2. The slope values, $\frac{d(\Delta f_0)}{df_0}$, for these 7 core plugs are plotted against the absolute value of the volume susceptibility difference between the rock matrix and water in Fig. 4. As predicted from Eq. (12), the plot is linear with an intercept near zero.

5.3. 3D Centric Scan SPRITE imaging of brine saturated rock cores

Prediction of the optimal field based on the variation of $1/T_2^*$ over a range of frequencies can be utilized to choose an appropriate field for rock core plug SPRITE imaging. The local image intensity, Eq. (1), features a T_2^* decay term. Decreased T_2^* due to magnetic susceptibility effects which are field dependent will yield decreased image intensity as B_0 increases. However, ρ_0 will increase as B_0 increases. In this section we consider SPRITE imaging with a common instrument, a common set of RF probes, common pulse programs, and common parameters to image a suitable cohort of samples as a function of field B_0.

Fig. 5 shows 2D slices extracted from 3D Centric Scan SPRITE images at 1.5 T and 3 T of Bentheimer, Nugget, Buff Berea, Berea,

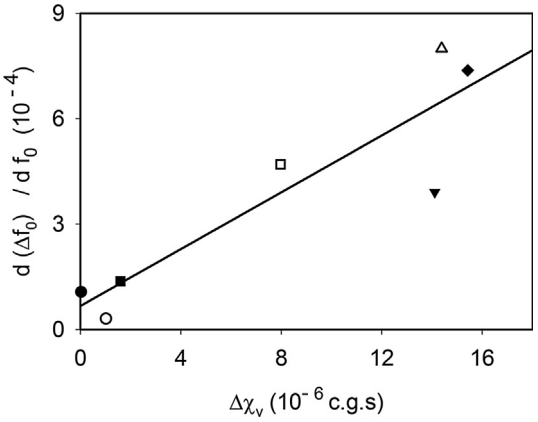

Fig. 4. $\frac{d(\Delta f_0)}{df_0}$ versus the absolute volume magnetic susceptibility difference between the pore filling water and solid rock matrix for (●) Rock 174S, (■) Rock 39A, (○) Rock MIT, (□) Rock 92A, (▼) Rock 4, (Δ) Rock W001, and (◆) Rock 18A. The $\frac{d(\Delta f_0)}{df_0}$ values utilized in this figure are the slopes from a linear fit to the data of $\Delta f_0 = 1/(\pi T_2^*)$ over a range of frequencies, f_0. The slope values are reported in Table 2 for the above seven rock core plugs.

and Wallace core plugs. The signal intensity is normalized to the maximum signal intensity of the Bentheimer core plug image at 3 T. The SNR from the Bentheimer sample was 210 at 3 T. In the SPRITE images, the background noise differed by 10% at the two magnetic fields (3 T and 1.5 T). The background noise was identical for all core plug images at a specific field. Note that a 10% difference between the background noise of the two magnetic fields is not apparent in the display of Fig. 5. The Centric Scan SPRITE images are remarkably uniform macroscopically. Microscopically all samples are heterogeneous since they have pore size distributions revealed in the T_1/T_2 behavior.

The image SNR varies due to magnetic field dependent variations in T_2^*, sample magnetization differences with B_0, and porosity differences between the core plugs in the SPRITE images of all core plugs. For the Bentheimer, Nugget, and Buff Berea core plugs, which have generally longer T_2^*, the image SNR increased as B_0 field increased (Table 4). The difference in the image SNR at the two magnetic fields for the Berea core plug is not statistically significant. The short T_2^* lifetime of fluid in the Wallace core plug at 3 T diminished the sensitivity of the SPRITE measurement compared to the same sample at 1.5 T by a factor of two. Table 4 lists the sensitivity and SNR corresponding to each sample at both magnetic fields.

The Centric Scan SPRITE technique is a naturally quantitative measurement [8,24]. The local image intensity at any point in the image is proportional to the magnetization, and thus proton density ρ_0 in Eq. (1) [8,24]. The local signal intensity is reduced only by $\exp(-t_p/T_2^*)$ ($\sin\alpha$ assumed constant), with T_2^* as a contrast parameter. For the Bentheimer, Nugget, and Buff Berea core plugs, the T_2^* is sufficiently long to avoid significant T_2^* attenuation, with a typical t_p of 100 μs. In addition, the field dependent sample magnetization, which is proportional to the proton density ρ_0, dominates over the decay term (Eq. (1)) at 3 T. As a consequence, SNR is higher in the SPRITE images of the above core plug samples at 3 T (Table 4).

Table 4
Comparison of the image SNR and sensitivity of Centric Scan SPRITE imaging at 1.5 T and 3 T for the five brine saturated rock core plugs.

	1.5 T		3 T	
	SNR	Sensitivity ($min^{-1/2}$)	SNR	Sensitivity ($min^{-1/2}$)
Bentheimer	140	26	210	38
Nugget	97	21	110	24
Buff Berea	110	24	160	32
Berea	75	17	78	17
Wallace	21	4	10	22

For the Berea core plug, however, magnetization is greater at 3 T, but the T_2^* is shorter, 98 μs. At lower field the sample magnetization is decreased but T_2^* is longer, 170 μs. In this case, one compensates for the other, resulting in a similar SNR at both magnetic fields (Table 4). For the Wallace sample, with more significant susceptibility mismatch, the very short T_2^*, 34 μs, at 3 T yields an SNR of 10. At 1.5 T, where T_2^* is longer, 57 μs, SNR increases by a factor of two, SNR = 21.

Fig. 6a and b show 2D slices extracted from a 3D Centric Scan SPRITE image of the Wallace sandstone at 3 T and 0.2 T. 64 signal averages were acquired for these two images. For the Wallace sandstone image at 3 T, the SNR was 6, Table 5. Signal and noise are both apparent in the image of Fig. 6a. The SNR was 46 for the Wallace sandstone image at 0.2 T. Noise is mapped to the minimum range in the scale bar of Fig. 6b.

At 0.2 T, the B_0 field and thus the sample magnetization is less than at 3 T by one order of magnitude. However, the T_2^* is much longer, 390 μs, due to a decrease in the susceptibility mismatch effect. This results in a sensitivity increase of a factor of five. The T_2^* in the Wallace sample at 3 T was very short, 34 μs, yielding a signal attenuation of e^{-3} with $t_p = 100$ μs. At 3 T, only 5% of the total signal remains after $t_p = 100$ μs. In contrast, with a $T_2^* = 390$ μs for the Wallace sample at 0.2 T, 78% of the signal remains after $t_p = 100$ μs. The use of a lower field magnet, 0.2 T, limits susceptibility mismatch effects. This results in a viable SPRITE MRI measurement.

The results of Fig. 5 are not intended to suggest that imaging is not possible at low field. Most of our own rock core imaging has

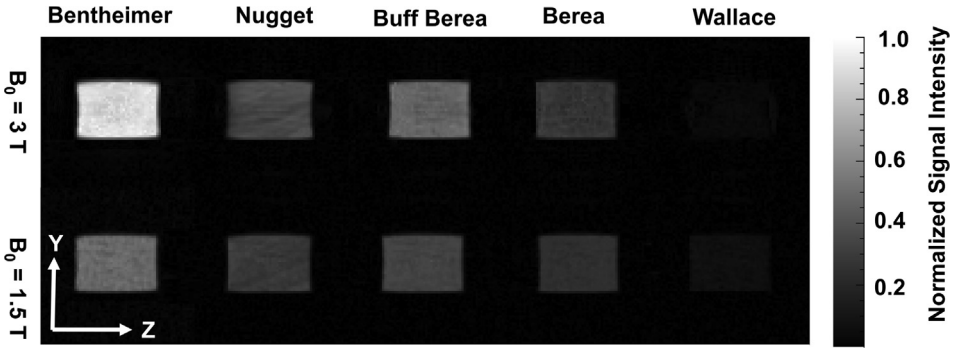

Fig. 5. 2D slices extracted from 3D SPRITE images at 1.5 T and 3 T, acquired with an encoding time of 100 μs, for different brine saturated core plugs. For each sample a slice from the center of the core plug image is displayed. The SNR is higher in the Bentheimer, Nugget, and Buff Berea core plug images at 3 T compared to 1.5 T while the Wallace sandstone images has greater SNR at 1.5 T.

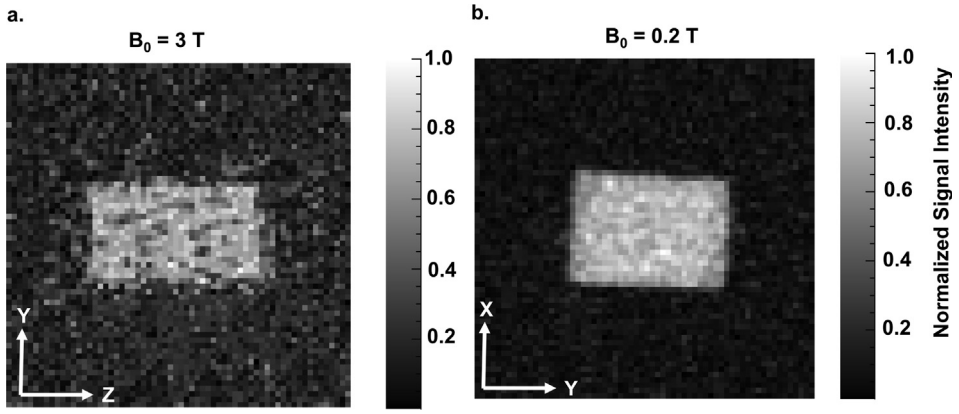

Fig. 6. **(a)** 2D slice from a 3D Centric scan SPRITE image of the Wallace core plug at 3 T with 64 signal averages. **(b)** 2D image extracted from a 3D SPRITE image of the Wallace core plug at 0.2 T with 64 signal averages. Note that these two images were acquired with two different instruments. The color bar next to each image indicates the magnitude of the signal intensity. The image SNR is higher by a factor of 8 at 0.2 T compared to 3 T due to the longer T_2^* lifetime.

Table 5
SNR and sensitivity of Centric Scan SPRITE images of the Wallace sandstone at 0.2 T and 3 T with 64 signal averages. The image SNR and sensitivity of the SPRITE measurements were higher at 0.2 T than at 3 T due to longer T_2^*.

	0.2 T		3 T	
	SNR	Sensitivity ($min^{-1/2}$)	SNR	Sensitivity ($min^{-1/2}$)
Wallace	46	2.5	6.0	0.50

been undertaken at 0.2 T [34–36]. We note that image SNR is the most reliable way to judge an acceptable fluid content, saturation, rock core image. Our results suggest that a SNR of 10 or better is a reasonable criteria for acceptance. The SNR may of course be improved by signal averaging. The sensitivity reported in Table 4 helps judge whether signal averaging is a fruitful strategy.

As discussed in Section 5.1, measurements on the variable field magnet in this work are coil noise dominated. Considering Eq. (6) for the coil noise regime, $SNR \propto B_0^{7/4} \exp(-t_p/T_2^*)$, $t_p = 100\ \mu s$, and T_2^* of the core plug samples at 3 T and 1.5 T, one can predict the SNR of the SPRITE images. For the Bentheimer core plug image, the SNR is predicted to be greater at 3 T than at 1.5 T by a factor of 3. Table 4, however, shows that the SNR is greater at 3 T than at 1.5 T by a factor of 1.5. In practice, different preamplifiers [37] and detection circuitry at the two fields may cause variation of the SNR from the predicted value. The same SNR prediction can be undertaken for the other core plug samples. The theoretical prediction in all cases over estimates the actual improvement. The prediction for the Wallace sandstone is problematic due to poor image SNR at each field.

6. Conclusion

The linear relationship between signal decay rate, $1/T_2^*$, and B_0 was confirmed experimentally for a variety of core plugs with disparate susceptibility difference, over a wide range of fields. This linear relationship was utilized to predict the optimal field strength in a Centric Scan SPRITE measurement. The maximum SNR is anticipated when $t_p = T_2^*$ and $t_p = 1.75\ T_2^*$ in the sample noise and the coil noise dominated regimes, respectively. When the sample and coil noise are comparable, the mixed noise regime, the maximum SNR is predicted for $t_p = 1.5\ T_2^*$. However, it is recommended that B_0 chosen to be less than the optimal field in order to increase T_2^* and ensure quantitative imaging in SPRITE measurements.

Variable field operation permits maximizing the sample magnetization while controlling the effect of susceptibility mismatch on the signal lifetimes in rock core plug samples. In SPRITE measurements, the image SNR is a balance between sample magnetization which increases with B_0, and T_2^* reduction as the field increases.

In this work we determine three simple experimental steps that permit the experimentalist to choose the optimal field for SPRITE MRI measurements of petroleum reservoir core plugs. These steps are (1) Determine the slope of $1/T_2^*$ versus B_0 field, potentially employing only one field for measurement. (2) Determine the noise regime for the sample and RF probe (s) to be employed. (3) Determine the acceptable level of T_2^* contrast in the resultant images. While the above procedure and discussion have been predicated on measurements of petroleum reservoir core plugs, the procedures are generic for other fluid saturated porous media.

A follow up study will be undertaken on a similar cohort of samples, focused on determining the optimal field for Fast Spin Echo (FSE) [30,38] MR imaging. Since T_2 is multi exponential and does not vary with B_0 in a simple manner, FSE imaging contrast will be more complicated than for Centric Scan SPRITE. Nevertheless, there is still merit in predicting the optimal field in rock core FSE imaging due to its high sensitivity. FSE images are very informative in terms of macroscopic structural heterogeneity. The optimal field in FSE core plug imaging methods is anticipated to be sample dependent.

Acknowledgement

B.J. Balcom thanks NSERC of Canada for a Discovery grant and the Canada Chairs program for a Research Chair in MRI of Materials. BJB also thank Green Imaging Technologies, ConocoPhillips, Saudi Aramco, the Atlantic Innovation Fund and the New Brunswick Innovation Fund for financial support. R. Enjilela also thanks Dr. Florin Marica and Dr. Ruslan Garipov from MR Solutions for helpful discussions. This paper is dedicated to the memory of our colleague Micheal McAloon who commenced this investigation but died in December 2009.

Funding

This study was funded by an NSERC Discovery grant (grant number 2015-6122), CRC grant (grant number 950-230894), AIF grant (grant number 201220), and NBIF-RAI: 2017-2018 held by Dr. B.J. Balcom.

Declaration of Competing Interest

None.

References

[1] Q. Chen, A.E. Marble, B.G. Colpitts, B.J. Balcom, The internal magnetic field distribution, and single exponential magnetic resonance free induction decay, in rocks, J. Magn. Reson. 175 (2005) 300–308, https://doi.org/10.1016/j.jmr.2005.05.001.

[2] J. Mitchell, T.C. Chandrasekera, D.J. Holland, L.F. Gladden, E.J. Fordham, Magnetic resonance imaging in laboratory petrophysical core analysis, Phys. Rep. 526 (2013) 165–225, https://doi.org/10.1016/j.physrep.2013.01.003.

[3] J. Mitchell, Rapid measurements of heterogeneity in sandstones using low-field nuclear magnetic resonance, J. Magn. Reson. 240 (2014) 52–60, https://doi.org/10.1016/j.jmr.2014.01.006.

[4] O.V. Petrov, B.J. Balcom, Two-dimensional T_2 distribution mapping in porous solids with phase encode MRI, J. Magn. Reson. 212 (2011) 102–108, https://doi.org/10.1016/j.jmr.2011.06.018.

[5] S. Vashaee, M. Li, B. MacMillan, R. Enjilela, D.P. Green, F. Marica, B.J. Balcom, Magnetic resonance imaging with a variable field superconducting magnet that can be rotated for vertical or horizontal operation, in: International Symposium of the Society of Core Analysts, Vienna, Austria, 2017, August 28-31, pp. 102–108.

[6] F. Marica, Q. Chen, A. Hamilton, C. Hall, T. Al, B.J. Balcom, Spatially resolved measurement of rock core porosity, J. Magn. Reson. 178 (2006) 136–141, https://doi.org/10.1016/j.jmr.2005.09.003.

[7] R.L. Kleinberg, W.E. Kenyon, P.P. Mitra, Mechanism of NMR relaxation of fluids in rock, J. Magn. Reson. Ser. A. 108 (1994) 206–214.

[8] M. Halse, D.J. Goodyear, B. MacMillan, P. Szomolanyi, D. Matheson, B.J. Balcom, Centric scan SPRITE magnetic resonance imaging, J. Magn. Reson. 165 (2003) 219–229, https://doi.org/10.1016/j.jmr.2003.08.004.

[9] J. Mitchell, J. Staniland, R. Chassagne, K. Mogensen, S. Frank, E.J. Fordham, Mapping oil saturation distribution in a limestone plug with low-field magnetic resonance, J. Pet. Sci. Eng. 108 (2013) 14–21, https://doi.org/10.1016/j.petrol.2013.04.008.

[10] C. Straley, D. Rossini, H. Vinegar, P. Tutunjian, C. Morriss, Core analysis by low field NMR, Log Anal. 38 (1997) 84–93.

[11] J. Mitchell, T.C. Chandrasekera, M.L. Johns, L.F. Gladden, E.J. Fordham, Nuclear magnetic resonance relaxation and diffusion in the presence of internal gradients: The effect of magnetic field strength, Phys. Rev. E. E 81 (0261) (2010) 1–19, https://doi.org/10.1103/PhysRevE.81.026101.

[12] H.-U. Kauczor, K.-F. Kreitner, MRI of the pulmonary parenchyma, Eur. Radiol. 9 (1999) 1755–1764.

[13] M.S. Conradi, B.T. Saam, D.A. Yablonskiy, J.C. Woods, Hyperpolarized ^{3}He and perfluorocarbon gas diffusion MRI of lungs, Prog. Nucl. Magn. Reson. Spectrosc. 48 (2006) 63–83, https://doi.org/10.1016/j.pnmrs.2005.12.001.

[14] J. Parra-Robles, A.R. Cross, G.E. Santyr, Theoretical signal-to-noise ratio and spatial resolution dependence on the magnetic field strength for hyperpolarized noble gas magnetic resonance imaging of human lungs, Med. Phys. 32 (2005) 221–229, https://doi.org/10.1118/1.1833593.

[15] J. Mitchell, L.F. Gladden, T.C. Chandrasekera, E.J. Fordham, Low-field permanent magnets for industrial process and quality control, Prog. Nucl. Magn. Reson. Spectrosc. 76 (2014) 1–60, https://doi.org/10.1016/j.pnmrs.2013.09.001.

[16] R.M. Weisskof, C.S. Zuo, J.L. Boxerman, B.R. Rosen, Microscopic susceptibility variation and transverse relaxation: theory and experiment, Magn. Reson. Med. 31 (1994) 601–610.

[17] P. Callaghan, Susceptibility-limited resolution in nuclear magnetic resonance microscopy, J. Magn. Reson. 87 (1990) 304–318, https://doi.org/10.1016/0022-2364(90)90007-V.

[18] Q. Chen, M. Halse, B.J. Balcom, Centric scan SPRITE for spin density imaging of short relaxation time porous materials, Magn. Reson. Imaging. 23 (2005) 263–266, https://doi.org/10.1016/j.mri.2004.11.020.

[19] K.R. Minard, R.A. Wind, Solenoidal microcoil design – Part II: Optimizing winding parameters for maximum signal-to-noise performance, Concepts Magn. Reson. 13 (2001) 190–210, https://doi.org/10.1002/Cmr.1008.

[20] W.A. Edelstein, G.H. Glover, C.J. Hardy, R.W. Redington, The intrinsic signal-to-noise ratio in NMR imaging, Magn. Reson. Med. 3 (1986) 604–618, https://doi.org/10.1002/mrm.1910030413.

[21] O. Ocali, E. Atalar, Ultimate intrinsic signal-to-noise ratio in MRI, Magn. Reson. Med. 39 (1998) 462–473, https://doi.org/10.1002/mrm.1910390317.

[22] D.I. Hoult, R.E. Richards, The Signal-to-Noise Ratio of the nuclear magnetic resonance experiment, J. Magn. Reson. 24 (1976) 71–85, https://doi.org/10.1016/0022-2364(76)90233-X.

[23] F.D. Doty, G. Entzminger, J. Kulkarni, K. Pamarthy, J.P. Staab, Radio frequency coil technology for small-animal MRI, NMR Biomed. 20 (2007) 304–325, https://doi.org/10.1002/nbm.

[24] Q. Chen, F.R. Rack, B.J. Balcom, Quantitative magnetic resonance imaging methods for core analysis, Geol. Soc. Special Publ. 267 (2006) 193–207, https://doi.org/10.1144/GSL.SP.2006.267.01.14.

[25] C.E. Muir, B.J. Balcom, Pure phase encode magnetic resonance imaging of fluids in porous media, in: Annu. Reports NMR Spectrosc., first ed., Academic Press, Burlington, USA, 2012, pp. 81–113. doi: 10.1016/B978-0-12-397020-6.00002-7.

[26] D.I. Hoult, The Nmr receiver: a description and analysis of design, Prog. NMR Spectrosc. 12 (1978) 41–77.

[27] D.I. Hoult, P.C. Lauterbur, The sensitivity of the zeugmatographic experiment involving human samples, J. Magn. Reson. 34 (1979) 425–433, https://doi.org/10.1016/0022-2364(79)90019-2.

[28] H.D.W. Hill, R.E. Richards, Limits of measurement in magnetic resonance, J. Phys. E Sci. Instrum. 1 (1968) 977–1083.

[29] A.G. Webb (Ed.), Magnetic Resonance Technology Hardware and System Component Design, The Royal Society of Chemistry, Cambridge, UK, 2016, doi: 10.1039/9781782623878.

[30] J. Mitchell, E.J. Fordham, Nuclear magnetic resonance core analysis at 0.3 T, Rev. Sci. Instrum. 85 111502 (2014), https://doi.org/10.1063/1.4902093.

[31] Magnetic susceptibility balance, instruction manual, Sherwood Scientific LTD (2005) 1–27.

[32] J. Mispelter, M. Lupu, A. Briguet, NMR probeheads for biophysical and biomedical experiments: theoretical principles & practical guidelines, first ed., Imperial Colloge Press, London, UK, 2006.

[33] E.G. Manger, Porosity and bulk density of sedimentary rocks, Geol. Surv. Bull. 1144-E (1963) 23–55.

[34] F. Marica, F.G. Goora, B.J. Balcom, FID-SPI pulse sequence for quantitative MRI of fluids in porous media, J. Magn. Reson. 240 (2014) 61–66, https://doi.org/10.1016/j.jmr.2014.01.003.

[35] S. Vashaee, O.V. Petrov, B.J. Balcom, B. Newling, Region of interest selection of long core plug samples by magnetic resonance imaging: profiling and local T_2 measurement, Measure. Sci. Technol. 25 (2014), https://doi.org/10.1088/0957-0233/25/3/035004 035004.

[36] M. Li, D. Xiao, L. Romero-Zerón, F. Marica, B. MacMillan, B.J. Balcom, Mapping three-dimensional oil distribution with π-EPI MRI measurements at low magnetic field, J. Magn. Reson. 269 (2016) 13–23, https://doi.org/10.1016/j.jmr.2016.05.008.

[37] D.R. Straw (Ed.), The ARRL Handbook for Radio Amateurs, 76th ed., American Radio Relay League Inc., Newington, CT, USA, 1998.

[38] J. Hennig, A. Nauerth, H. Friedburg, RARE imaging: a fast imaging method for clinical MR, Magn. Reson. Med. 3 (1986) 823–833.